Cross sections for the reactions e[superscript +]e[superscript −] → K[superscript 0][subscript S]K[superscript 0][subscript L]π[superscript 0], K[superscript 0][subscript S]K[superscript 0][subscript L]# , and K[superscript 0][subscript S]K[superscript 0][subscript L]π[superscript 0]π[superscript 0] from events with initial-state radiation

Cross sections for the reactions $e^+e^- \to K^0_S K^0_L \pi^0$, $K^0_S K^0_L \eta$, and $K^0_S K^0_L \pi^0 \pi^0$ from events with initial-state radiation

J. P. Lees,[1] V. Poireau,[1] V. Tisserand,[1] E. Grauges,[2] A. Palano,[3] G. Eigen,[4] D. N. Brown,[5] Yu. G. Kolomensky,[5] M. Fritsch,[6] H. Koch,[6] T. Schroeder,[6] C. Hearty,[7a,7b] T. S. Mattison,[7b] J. A. McKenna,[7b] R. Y. So,[7b] V. E. Blinov,[8a,8b,8c] A. R. Buzykaev,[8a] V. P. Druzhinin,[8a,8b] V. B. Golubev,[8a,8b] E. A. Kravchenko,[8a,8b] A. P. Onuchin,[8a,8b,8c] S. I. Serednyakov,[8a,8b] Yu. I. Skovpen,[8a,8b] E. P. Solodov,[8a,8b] K. Yu. Todyshev,[8a,8b] A. J. Lankford,[9] J. W. Gary,[10] O. Long,[10] A. M. Eisner,[11] W. S. Lockman,[11] W. Panduro Vazquez,[11] D. S. Chao,[12] C. H. Cheng,[12] B. Echenard,[12] K. T. Flood,[12] D. G. Hitlin,[12] J. Kim,[12] T. S. Miyashita,[12] P. Ongmongkolkul,[12] F. C. Porter,[12] M. Röhrken,[12] Z. Huard,[13] B. T. Meadows,[13] B. G. Pushpawela,[13] M. D. Sokoloff,[13] L. Sun,[13,*] J. G. Smith,[14] S. R. Wagner,[14] D. Bernard,[15] M. Verderi,[15] D. Bettoni,[16a] C. Bozzi,[16a] R. Calabrese,[16a,16b] G. Cibinetto,[16a,16b] E. Fioravanti,[16a,16b] I. Garzia,[16a,16b] E. Luppi,[16a,16b] V. Santoro,[16a] A. Calcaterra,[17] R. de Sangro,[17] G. Finocchiaro,[17] S. Martellotti,[17] P. Patteri,[17] I. M. Peruzzi,[17] M. Piccolo,[17] M. Rotondo,[17] A. Zallo,[17] S. Passaggio,[18] C. Patrignani,[18,†] H. M. Lacker,[19] B. Bhuyan,[20] U. Mallik,[21] C. Chen,[22] J. Cochran,[22] S. Prell,[22] H. Ahmed,[23] A. V. Gritsan,[24] N. Arnaud,[25] M. Davier,[25] F. Le Diberder,[25] A. M. Lutz,[25] G. Wormser,[25] D. J. Lange,[26] D. M. Wright,[26] J. P. Coleman,[27] E. Gabathuler,[27,‡] D. E. Hutchcroft,[27] D. J. Payne,[27] C. Touramanis,[27] A. J. Bevan,[28] F. Di Lodovico,[28] R. Sacco,[28] G. Cowan,[29] Sw. Banerjee,[30] D. N. Brown,[30] C. L. Davis,[30] A. G. Denig,[31] W. Gradl,[31] K. Griessinger,[31] A. Hafner,[31] K. R. Schubert,[31] R. J. Barlow,[32,§] G. D. Lafferty,[32] R. Cenci,[33] A. Jawahery,[33] D. A. Roberts,[33] R. Cowan,[34] S. H. Robertson,[35] B. Dey,[36a] N. Neri,[36a] F. Palombo,[36a,36b] R. Cheaib,[37] L. Cremaldi,[37] R. Godang,[37,‖] D. J. Summers,[37] P. Taras,[38] G. De Nardo,[39] C. Sciacca,[39] G. Raven,[40] C. P. Jessop,[41] J. M. LoSecco,[41] K. Honscheid,[42] R. Kass,[42] A. Gaz,[43a] M. Margoni,[43a,43b] M. Posocco,[43a] G. Simi,[43a,43b] F. Simonetto,[43a,43b] R. Stroili,[43a,43b] S. Akar,[44] E. Ben-Haim,[44] M. Bomben,[44] G. R. Bonneaud,[44] G. Calderini,[44] J. Chauveau,[44] G. Marchiori,[44] J. Ocariz,[44] M. Biasini,[45a,45b] E. Manoni,[45a] A. Rossi,[45a] G. Batignani,[46a,46b] S. Bettarini,[46a,46b] M. Carpinelli,[46a,46b,**] G. Casarosa,[46a,46b] M. Chrzaszcz,[46a] F. Forti,[46a,46b] M. A. Giorgi,[46a,46b] A. Lusiani,[46a,46c] B. Oberhof,[46a,46b] E. Paoloni,[46a,46b] M. Rama,[46a] G. Rizzo,[46a,46b] J. J. Walsh,[46a] A. J. S. Smith,[47] F. Anulli,[48a] R. Faccini,[48a,48b] F. Ferrarotto,[48a] F. Ferroni,[48a,48b] A. Pilloni,[48a,48b] G. Piredda,[48a,‡] C. Bünger,[49] S. Dittrich,[49] O. Grünberg,[49] M. Heß,[49] T. Leddig,[49] C. Voß,[49] R. Waldi,[49] T. Adye,[50] F. F. Wilson,[50] S. Emery,[51] G. Vasseur,[51] D. Aston,[52] C. Cartaro,[52] M. R. Convery,[52] J. Dorfan,[52] W. Dunwoodie,[52] M. Ebert,[52] R. C. Field,[52] B. G. Fulsom,[52] M. T. Graham,[52] C. Hast,[52] W. R. Innes,[52] P. Kim,[52] D. W. G. S. Leith,[52] S. Luitz,[52] D. B. MacFarlane,[52] D. R. Muller,[52] H. Neal,[52] B. N. Ratcliff,[52] A. Roodman,[52] M. K. Sullivan,[52] J. Va'vra,[52] W. J. Wisniewski,[52] M. V. Purohit,[53] J. R. Wilson,[53] A. Randle-Conde,[54] S. J. Sekula,[54] M. Bellis,[55] P. R. Burchat,[55] E. M. T. Puccio,[55] M. S. Alam,[56] J. A. Ernst,[56] R. Gorodeisky,[57] N. Guttman,[57] D. R. Peimer,[57] A. Soffer,[57] S. M. Spanier,[58] J. L. Ritchie,[59] R. F. Schwitters,[59] J. M. Izen,[60] X. C. Lou,[60] F. Bianchi,[61a,61b] F. De Mori,[61a,61b] A. Filippi,[61a] D. Gamba,[61a,61b] L. Lanceri,[62] L. Vitale,[62] F. Martinez-Vidal,[63] A. Oyanguren,[63] J. Albert,[64b] A. Beaulieu,[64b] F. U. Bernlochner,[64b] G. J. King,[64b] R. Kowalewski,[64b] T. Lueck,[64b] I. M. Nugent,[64b] J. M. Roney,[64b] R. J. Sobie,[64a,64b] N. Tasneem,[64b] T. J. Gershon,[65] P. F. Harrison,[65] T. E. Latham,[65] R. Prepost,[66] and S. L. Wu[66]

(*BABAR* Collaboration)

[1]*Laboratoire d'Annecy-le-Vieux de Physique des Particules (LAPP), Université de Savoie, CNRS/IN2P3, F-74941 Annecy-Le-Vieux, France*
[2]*Universitat de Barcelona, Facultat de Fisica, Departament ECM, E-08028 Barcelona, Spain*
[3]*INFN Sezione di Bari and Dipartimento di Fisica, Università di Bari, I-70126 Bari, Italy*
[4]*University of Bergen, Institute of Physics, N-5007 Bergen, Norway*
[5]*Lawrence Berkeley National Laboratory and University of California, Berkeley, California 94720, USA*
[6]*Ruhr Universität Bochum, Institut für Experimentalphysik 1, D-44780 Bochum, Germany*
[7a]*Institute of Particle Physics, Vancouver, British Columbia, Canada V6T 1Z1*
[7b]*University of British Columbia, Vancouver, British Columbia, Canada V6T 1Z1*
[8a]*Budker Institute of Nuclear Physics SB RAS, Novosibirsk 630090, Russia*
[8b]*Novosibirsk State University, Novosibirsk 630090, Russia*
[8c]*Novosibirsk State Technical University, Novosibirsk 630092, Russia*
[9]*University of California at Irvine, Irvine, California 92697, USA*
[10]*University of California at Riverside, Riverside, California 92521, USA*
[11]*University of California at Santa Cruz, Institute for Particle Physics, Santa Cruz, California 95064, USA*
[12]*California Institute of Technology, Pasadena, California 91125, USA*
[13]*University of Cincinnati, Cincinnati, Ohio 45221, USA*
[14]*University of Colorado, Boulder, Colorado 80309, USA*
[15]*Laboratoire Leprince-Ringuet, Ecole Polytechnique, CNRS/IN2P3, F-91128 Palaiseau, France*
[16a]*INFN Sezione di Ferrara, I-44122 Ferrara, Italy*

[16b]*Dipartimento di Fisica e Scienze della Terra, Università di Ferrara, I-44122 Ferrara, Italy*
[17]*INFN Laboratori Nazionali di Frascati, I-00044 Frascati, Italy*
[18]*INFN Sezione di Genova, I-16146 Genova, Italy*
[19]*Humboldt-Universität zu Berlin, Institut für Physik, D-12489 Berlin, Germany*
[20]*Indian Institute of Technology Guwahati, Guwahati, Assam 781 039, India*
[21]*University of Iowa, Iowa City, Iowa 52242, USA*
[22]*Iowa State University, Ames, Iowa 50011, USA*
[23]*Physics Department, Jazan University, Jazan 22822, Kingdom of Saudi Arabia*
[24]*Johns Hopkins University, Baltimore, Maryland 21218, USA*
[25]*Laboratoire de l'Accélérateur Linéaire, IN2P3/CNRS et Université Paris-Sud 11, Centre Scientifique d'Orsay, F-91898 Orsay Cedex, France*
[26]*Lawrence Livermore National Laboratory, Livermore, California 94550, USA*
[27]*University of Liverpool, Liverpool L69 7ZE, United Kingdom*
[28]*Queen Mary, University of London, London E1 4NS, United Kingdom*
[29]*University of London, Royal Holloway and Bedford New College, Egham, Surrey TW20 0EX, United Kingdom*
[30]*University of Louisville, Louisville, Kentucky 40292, USA*
[31]*Johannes Gutenberg-Universität Mainz, Institut für Kernphysik, D-55099 Mainz, Germany*
[32]*University of Manchester, Manchester M13 9PL, United Kingdom*
[33]*University of Maryland, College Park, Maryland 20742, USA*
[34]*Massachusetts Institute of Technology, Laboratory for Nuclear Science, Cambridge, Massachusetts 02139, USA*
[35]*Institute of Particle Physics and McGill University, Montréal, Québec H3A 2T8, Canada*
[36a]*INFN Sezione di Milano, I-20133 Milano, Italy*
[36b]*Dipartimento di Fisica, Università di Milano, I-20133 Milano, Italy*
[37]*University of Mississippi, University, Mississippi 38677, USA*
[38]*Université de Montréal, Physique des Particules, Montréal, Québec H3C 3J7, Canada*
[39]*INFN Sezione di Napoli and Dipartimento di Scienze Fisiche, Università di Napoli Federico II, I-80126 Napoli, Italy*
[40]*NIKHEF, National Institute for Nuclear Physics and High Energy Physics, NL-1009 DB Amsterdam, Netherlands*
[41]*University of Notre Dame, Notre Dame, Indiana 46556, USA*
[42]*Ohio State University, Columbus, Ohio 43210, USA*
[43a]*INFN Sezione di Padova, I-35131 Padova, Italy*
[43b]*Dipartimento di Fisica, Università di Padova, I-35131 Padova, Italy*
[44]*Laboratoire de Physique Nucléaire et de Hautes Energies, IN2P3/CNRS, Université Pierre et Marie Curie-Paris6, Université Denis Diderot-Paris7, F-75252 Paris, France*
[45a]*INFN Sezione di Perugia, I-06123 Perugia, Italy*
[45b]*Dipartimento di Fisica, Università di Perugia, I-06123 Perugia, Italy*
[46a]*INFN Sezione di Pisa, I-56127 Pisa, Italy*
[46b]*Dipartimento di Fisica, Università di Pisa, I-56127 Pisa, Italy*
[46c]*Scuola Normale Superiore di Pisa, I-56127 Pisa, Italy*
[47]*Princeton University, Princeton, New Jersey 08544, USA*
[48a]*INFN Sezione di Roma, I-00185 Roma, Italy*
[48b]*Dipartimento di Fisica, Università di Roma La Sapienza, I-00185 Roma, Italy*
[49]*Universität Rostock, D-18051 Rostock, Germany*
[50]*Rutherford Appleton Laboratory, Chilton, Didcot, Oxon OX11 0QX, United Kingdom*
[51]*CEA, Irfu, SPP, Centre de Saclay, F-91191 Gif-sur-Yvette, France*
[52]*SLAC National Accelerator Laboratory, Stanford, California 94309, USA*
[53]*University of South Carolina, Columbia, South Carolina 29208, USA*
[54]*Southern Methodist University, Dallas, Texas 75275, USA*
[55]*Stanford University, Stanford, California 94305, USA*
[56]*State University of New York, Albany, New York 12222, USA*
[57]*Tel Aviv University, School of Physics and Astronomy, Tel Aviv 69978, Israel*
[58]*University of Tennessee, Knoxville, Tennessee 37996, USA*
[59]*University of Texas at Austin, Austin, Texas 78712, USA*
[60]*University of Texas at Dallas, Richardson, Texas 75083, USA*
[61a]*INFN Sezione di Torino, I-10125 Torino, Italy*
[61b]*Dipartimento di Fisica, Università di Torino, I-10125 Torino, Italy*
[62]*INFN Sezione di Trieste and Dipartimento di Fisica, Università di Trieste, I-34127 Trieste, Italy*

[63]IFIC, Universitat de Valencia-CSIC, E-46071 Valencia, Spain
[64a]Institute of Particle Physics, Victoria, British Columbia V8W 3P6, Canada
[64b]University of Victoria, Victoria, British Columbia V8W 3P6, Canada
[65]Department of Physics, University of Warwick, Coventry CV4 7AL, United Kingdom
[66]University of Wisconsin, Madison, Wisconsin 53706, USA
(Received 2 February 2017; published 6 March 2017)

We study the processes $e^+e^- \to K^0_S K^0_L \pi^0 \gamma$, $K^0_S K^0_L \eta\gamma$, and $K^0_S K^0_L \pi^0 \pi^0 \gamma$, where the photon is radiated from the initial state, providing cross section measurements for the hadronic final states over a continuum of center-of-mass energies. The results are based on 469 fb^{-1} of data collected at or near the $\Upsilon(4S)$ resonance with the *BABAR* detector at SLAC. We present the first measurements of the $e^+e^- \to K^0_S K^0_L \pi^0$, $K^0_S K^0_L \eta$, and $K^0_S K^0_L \pi^0 \pi^0$ cross sections up to a center-of-mass energy of 4 GeV and study their intermediate resonance structures. We observe J/ψ decays to all of these final states for the first time, present measurements of their J/ψ branching fractions, and search for $\psi(2S)$ decays.

DOI: 10.1103/PhysRevD.95.052001

I. INTRODUCTION

Electron-positron annihilation events with initial-state radiation (ISR) can be used to study processes over a wide range of energies below the nominal e^+e^- center-of-mass (c.m.) energy ($E_{\rm c.m.}$), as demonstrated in Ref. [1]. The possibility of exploiting ISR to make precise measurements of low-energy cross sections at high-luminosity ϕ and B factories is discussed in Refs. [2–4] and motivates the studies described in this paper. Such measurements are of particular current interest because of a three-standard-deviation discrepancy between the measured value of the muon anomalous magnetic moment $(g_\mu - 2)$ and that computed in the Standard Model [5], where the hadronic loop contributions require experimental e^+e^- annihilation cross sections as input. The calculation is most sensitive to the low-energy region, where the inclusive hadronic cross section cannot be measured reliably, and a sum of exclusive states must be used. Not all accessible states have been measured yet, and new measurements will improve the reliability of the calculation. In addition, studies of ISR events at B factories provide information on resonance spectroscopy for masses up through the charmonium region.

Studies of the ISR processes $e^+e^- \to \mu^+\mu^-\gamma$ [6,7] and $e^+e^- \to X_h\gamma$, where X_h represents any of several exclusive multihadron final states, using data of the *BABAR* experiment at SLAC, have been reported previously. The X_h studied so far include charged hadron pairs $\pi^+\pi^-$ [7], K^+K^- [8], and $p\bar{p}$ [9]; four or six charged mesons [10–12]; charged mesons plus one or two π^0 mesons [11–14]; a K^0_S plus charged and neutral mesons [15]; and the first ISR measurement from *BABAR* that includes K^0_L mesons [16]. Together, they demonstrate good detector efficiency for events of this kind and well-understood tracking, particle identification, and π^0, K^0_S and K^0_L reconstruction.

In this paper we report measurements of the $K^0_S K^0_L \pi^0$, $K^0_S K^0_L \eta$, and $K^0_S K^0_L \pi^0 \pi^0$ final states, produced in conjunction with a hard photon that is assumed to result from ISR. Candidate K^0_S mesons are reconstructed in the $\pi^+\pi^-$ decay mode, candidate π^0 and η mesons are reconstructed in the $\gamma\gamma$ decay mode, and K^0_L mesons are detected via their nuclear interactions in the electromagnetic calorimeter. For these final states, we measure cross sections from threshold to $E_{\rm c.m.} = 4$ GeV, study their internal structure, perform the first measurements of J/ψ branching fractions, and search for $\psi(2S)$ decays. We also search for the $e^+e^- \to \gamma K^0_S K^0_S \pi^0$ and $e^+e^- \to \gamma K^0_S K^0_S \pi^0 \pi^0$ processes, which are forbidden by C-parity conservation, and we see no indication of them at the level of single background events. Together with our previous measurements [8,11,16], these results provide a much more complete understanding of the $K\bar{K}\pi$, $K\bar{K}\eta$ and $K\bar{K}\pi\pi$ final states in e^+e^- annihilation.

II. THE *BABAR* DETECTOR AND DATA SET

The data used in this analysis were collected with the *BABAR* detector at the PEP-II2 asymmetric-energy e^+e^- storage ring. The total integrated luminosity used is 468.6 fb^{-1} [17], which includes data collected at the $\Upsilon(4S)$ resonance (424.7 fb^{-1}) and at a c.m. energy 40 MeV below this resonance (43.9 fb^{-1}).

The *BABAR* detector is described in detail elsewhere [18]. Charged particles are reconstructed using the *BABAR* tracking system, which comprises the silicon vertex tracker (SVT) and the drift chamber (DCH) inside the 1.5 T solenoid. Separation of pions and kaons is accomplished by

[*]Present address: Wuhan University, Wuhan 43072, China.
[†]Present address: Università di Bologna and INFN Sezione di Bologna, I-47921 Rimini, Italy.
[‡]Deceased.
[§]Present address: University of Huddersfield, Huddersfield HD1 3DH, United Kingdom.
[‖]Present address: University of South Alabama, Mobile, AL 36688, USA.
[**]Also at Università di Sassari, I-07100 Sassari, Italy.

means of the detector of internally reflected Cherenkov light and energy-loss measurements in the SVT and DCH. The hard ISR photon, photons from π^0 and η decays, and K_L^0 are detected in the electromagnetic calorimeter (EMC). Muon identification, provided by the instrumented flux return, is used to select the $\mu^+\mu^-\gamma$ final state.

To study the detector acceptance and efficiency, we have developed a special package of simulation programs for radiative processes based on the approach suggested by Kühn and Czyż [19]. Multiple collinear soft-photon emission from the initial e^+e^- state is implemented with the structure-function technique [20,21], while additional photon radiation from the final-state particles is simulated using the PHOTOS package [22]. The precision of the radiative simulation contributes less than 1% to the uncertainty of the measured hadronic cross sections.

In addition to the signal channels $K_S^0K_L^0\pi^0$, $K_S^0K_L^0\eta$, and $K_S^0K_L^0\pi^0\pi^0$, we simulate ISR processes which result in high backgrounds, $K_S^0K_L^0$, $K_S^0K^\pm\pi^\mp$, and $K_S^0K^\pm\pi^\mp\pi^0$, with cross sections and mass dependences based on our previous measurements and isospin relations. The $K_S^0K_L^0$ and $K_S^0K_L^0\eta$ channels are dominated by $e^+e^- \to \gamma\phi$ and $\gamma\phi\eta$, respectively. Samples of 3–5 times the number of expected events are generated for each final state and processed through the detector response simulation [23]. These events are then reconstructed using the same software chain as the data.

We also simulate several non-ISR backgrounds, including $e^+e^- \to q\bar{q}$ ($q = u$, d, s, c) events using the Jetset7.4 [24] generator and $e^+e^- \to \tau^+\tau^-$ events using the KORALB [25] generator. Variations in detector and background conditions are taken into account.

III. EVENT SELECTION AND RECONSTRUCTION

We begin with events containing at least two charged particles and at least four clusters of energy deposits in contiguous crystals in the EMC. We then consider the cluster in the event with the highest energy in the e^+e^- c.m. frame as the ISR photon candidate and require $E^\gamma_{\rm c.m.} > 3$ GeV. Since the ISR photons are produced mostly along the beam line, this accepts only about 10% of the signal events, but in the selected events, the hadronic system is fully contained and can be studied reliably.

In these events, we reconstruct candidate K_S^0 decays to two charged pions from pairs of oppositely charged tracks not identified as electrons. They must have a well-reconstructed vertex between 0.1 and 40.0 cm in radial distance from the beam axis, and their total momentum must be consistent with the assumption that they originate from the interaction region. The $m(\pi^+\pi^-)$ invariant mass distribution for these K_S^0 candidates is shown in Fig. 1 for both data (points) and the $e^+e^- \to \gamma\phi \to \gamma K_S^0K_L^0$ simulation (histogram). The signal is very clean, and requiring $482 < m(\pi^+\pi^-) < 512$ MeV/c^2 (vertical lines in Fig. 1) accepts 98% of the signal events. We use the sidebands 472–482 and 512–522 MeV/c^2 to estimate the contributions from non-K_S^0 backgrounds, which are found to be negligible in all cases after final selection.

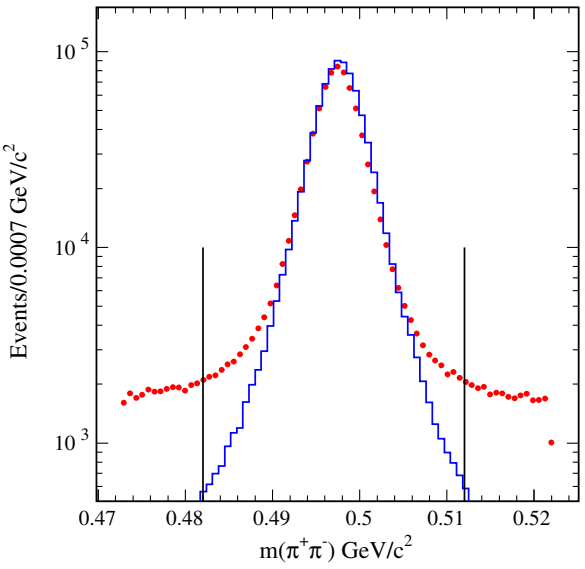

FIG. 1. The $\pi^+\pi^-$ invariant mass distribution for the selected K_S^0 candidates in the data (points) and simulation (histogram). The vertical lines indicate the signal region.

A few thousand events (about 1% of the total) have more than one selected K_S^0 candidate, and we use only the candidate with $m(\pi^+\pi^-)$ closest to the nominal [26] K_S^0 mass. We also require the event to contain no other tracks that extrapolate within 2 cm of the beam axis and 3 cm along the axis from the nominal interaction point.

Any number of additional tracks and EMC clusters is allowed. We consider all clusters with reconstructed energy above 0.1 GeV as photon candidates and calculate the invariant mass of each pair. Every pair with a mass within 30 (50) MeV/c^2 of the nominal π^0 (η) mass is considered a π^0 (η) candidate. The efficiency of π^0 and η reconstruction in these events is about 97%.

The decay length of the K_L^0 meson is large, and the probability to detect a K_L^0 decay in the DCH is low. Instead, we look for a cluster in the EMC resulting from the interaction of a K_L^0 with a nucleus in the EMC material. Such clusters are indistinguishable from photon-induced clusters and give poor resolution on the K_L^0 energy. The characteristics of these clusters were studied in detail in our previous publication [16], where it was shown using $e^+e^- \to \phi\gamma$ events that K_L^0 clusters are detected with high efficiency and good angular resolution. Background from low-energy clusters is high, and the requirement of at least 0.2 GeV in cluster energy yields a clean sample with 48% efficiency. Here, we apply the same energy requirement and use the efficiency and angular resolution measured as a function of polar and azimuthal angles in Ref. [16].

IV. THE KINEMATIC FIT PROCEDURE

Each event selected as described in Sec. III is subjected to a set of constrained kinematic fits, in which the four-momenta and covariance matrices of the initial e^+e^-, the ISR photon, the best K^0_S candidate, and zero, two or four relevant photon candidates are taken into account. The direction and angular resolution, but not the energy, of the K^0_L candidate is also used, and the K^0_L momentum is determined in the fit. The three-momentum vectors for all other particles, including the photons, are also determined with better accuracy from the fits, and the fitted values are used in further calculations.

For every event, we first perform kinematic fits under the $K^0_S K^0_L \gamma$ hypothesis, considering the ISR photon and K^0_S candidates, along with each cluster with energy over 0.2 GeV in turn as the K^0_L candidate. Each fit has three constraints, and we consider the combination with the best χ^2 value, denoted $\chi^2(K^0_S K^0_L)$. This variable is useful in suppressing the large background arising from combinations of background photons with a mass near the π^0 or η mass.

Next, we consider each π^0 and η candidate and perform a set of fits to the $K^0_S K^0_L \pi^0 \gamma$ and $K^0_S K^0_L \eta \gamma$ hypothesis, including the ISR photon, K^0_S, and two photon candidates, along with each K^0_L candidate not included in the π^0 or η candidate. These fits have four constraints, including one on the π^0 or η candidate mass. We retain the $\pi^0 K^0_L$ and ηK^0_L candidate combinations yielding the best values of $\chi^2(K^0_S K^0_L \pi^0)$ and $\chi^2(K^0_S K^0_L \eta)$, respectively.

Similarly, for events with six or more clusters, we consider each pair of nonoverlapping π^0 candidates and perform a set of five-constraint fits under the $K^0_S K^0_L \pi^0 \pi^0 \gamma$ hypothesis. Both π^0 masses are constrained, and we retain the $\pi^0 \pi^0 K^0_L$ candidate combination yielding the lowest value of $\chi^2(K^0_S K^0_L \pi^0 \pi^0)$.

Finally, we perform similar fits for all the other simulated signal and background processes discussed in Sec. II, giving us additional χ^2 variables that can be used to select (or suppress) these processes.

V. THE $K^0_S K^0_L \pi^0$ FINAL STATE

A. Additional selection criteria

For the $K^0_S K^0_L \pi^0$ final state, a few additional selection criteria are applied. Considering all pairs of EMC clusters not assigned to the ISR photon, π^0, or K^0_L candidates, we observe a large signal from extra π^0's, shown in Fig. 2. It is especially strong when one of the clusters has high energy, so we require $E^{\rm max}_\gamma < 0.5$ GeV. This reduces backgrounds from several sources with a loss of 3% in simulated signal efficiency. However, many ISR $\phi\gamma$ events with a false π^0, formed by accidental photons, remain. To reduce this background, we require $\chi^2(K^0_S K^0_L) > 15$ if the fitted $K^0_S K^0_L$ invariant mass $m(K^0_S K^0_L)$ is smaller than 1.04 GeV/c^2.

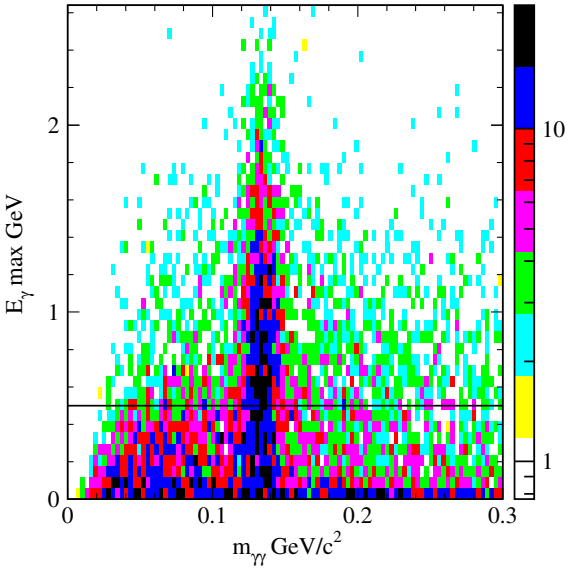

FIG. 2. Two-dimensional distribution of the higher cluster energy in a photon-candidate pair vs the corresponding diphoton mass $m_{\gamma\gamma}$ for all pairs of EMC clusters in $K^0_S K^0_L \pi^0 \gamma$ events containing neither the ISR photon, the K^0_L candidate, nor either photon in the π^0 candidate.

The 4C χ^2 distribution for the remaining events under the $K^0_S K^0_L \pi^0 \gamma$ hypothesis is shown as the points in Fig. 3(a), with the corresponding distribution for MC-simulated pure $K^0_S K^0_L \pi^0 \gamma$ events shown as the open histogram. Both distributions are broader than typical 4C χ^2 distributions due to higher-order ISR, which is present in both data and simulation but not taken into account in the fit. The reliability of the simulated distribution has been demonstrated in our previous studies and is discussed below. In the figure, the simulated signal distribution is normalized to the data in the region $\chi^2(K^0_S K^0_L \pi^0) < 3$, where the contribution of higher-order ISR is small and the background contamination is lowest, but still amounts to about 5% of the signal. The difference between the two distributions at high values gives an indication of the level of background.

We define a signal region $\chi^2(K^0_S K^0_L \pi^0) < 25$ and a control region $25 < \chi^2(K^0_S K^0_L \pi^0) < 50$ [vertical lines in Fig. 3(a)], from which we estimate backgrounds in the signal region. The signal region contains 5441 data and 3402 signal-MC events, while the control region contains 2733 and 632 events, respectively.

B. Background subtraction

We estimate known ISR backgrounds from simulation and normalize the simulated non-ISR background using the π^0 peak, as described in Ref. [16]. The largest backgrounds we can evaluate in this way are shown in Fig. 3(a): the shaded, cross-hatched, and hatched areas represent the simulated backgrounds from non-ISR $q\bar{q}$, ISR $K^0_S K^0_L(\phi)$, and ISR $\phi\eta$ events, respectively. The shapes of these three

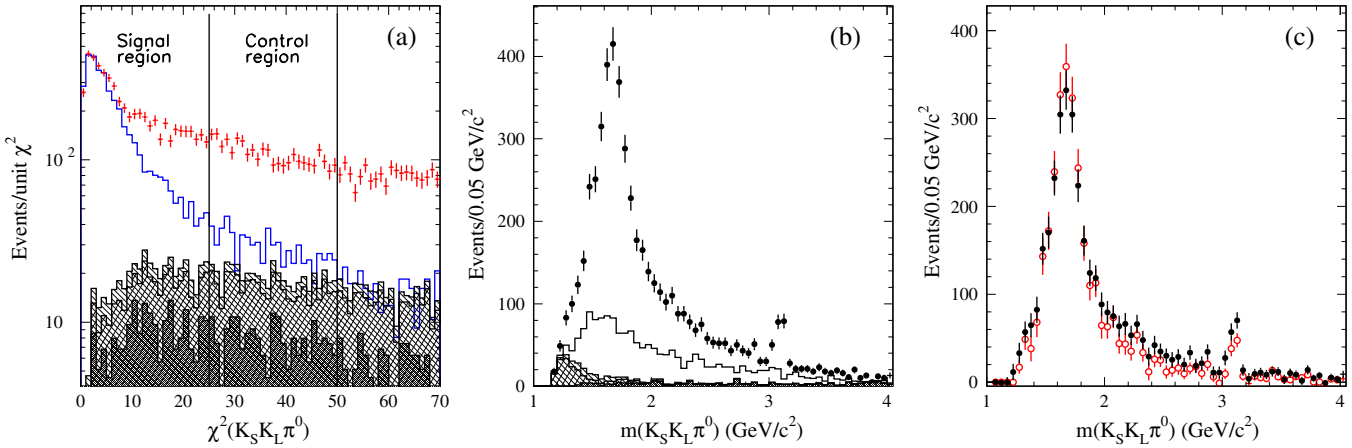

FIG. 3. (a) The four-constraint χ^2 distributions for data (points) and MC-simulated $K^0_SK^0_L\pi^0\gamma$ events (open histogram). The shaded, cross-hatched, and hatched areas represent the simulated backgrounds from non-ISR $q\bar{q}$, ISR ϕ, and ISR $\phi\eta$ events, respectively. (b) The $K^0_SK^0_L\pi^0$ invariant mass distribution for data events in the signal region (points). The shaded, cross-hatched, and hatched areas represent the simulated contributions from non-ISR $q\bar{q}$, ISR ϕ, and ISR $\phi\eta$ events, respectively, while the open histogram represents the total background estimated from the control region. (c) The $K^0_SK^0_L\pi^0$ invariant mass distribution after background subtraction (points). The open circles represent the contribution from the resonant process $e^+e^- \to K^*(892)^0\bar{K}^0 + \text{c.c.} \to K^0_SK^0_L\pi^0$ (see text).

distributions are consistent with each other and quite distinct from that expected for signal events. However, these backgrounds account for less than half of the observed difference between data and simulation at large χ^2 values. We assume the remaining background is from other ISR processes, with a $\chi^2(K^0_SK^0_L\pi^0)$ distribution similar in shape to those shown.

To obtain any distribution of the $K^0_SK^0_L\pi^0$ signal events, we use the control region to estimate the sum of all backgrounds, following the procedure described in detail in Ref. [16]. In each bin of the distribution in question, the background contribution is estimated as the difference between the numbers of data and signal-MC events in the control region [see Fig. 3(a)], normalized to the corresponding difference in the signal region.

The $K^0_SK^0_L\pi^0$ invariant mass distribution of events in the signal region is shown in Fig. 3(b) as the points. The shaded, cross-hatched, and hatched areas represent the same simulated backgrounds as in Fig. 3(a). The sum of all backgrounds, estimated from the control region, is shown as the open histogram in Fig. 3(b), and the extracted mass distribution for $e^+e^- \to K^0_SK^0_L\pi^0$ signal events is shown as the filled points in Fig. 3(c). We observe 3669 events in the mass range from threshold to 4.0 GeV/c^2. In addition to a main peak around 1.8 GeV/c^2, a J/ψ signal is visible.

This procedure relies on good agreement between data and simulation in the $\chi^2(K^0_SK^0_L\pi^0)$ distribution. Considering our previous studies of χ^2 distributions [16], along with simulation and normalization statistics, we estimate the relative systematic uncertainty on the background to be 30%. This results in an uncertainty on the background-subtracted signal of about 10% for $m(K^0_SK^0_L\pi^0) < 2.2$ GeV/c^2, increasing roughly linearly with mass to about 40% at 3.2 GeV/c^2 and above.

C. Detection efficiency

The selection procedures applied to the data are also applied to the MC-simulated event sample. The resulting distribution of the reconstructed $K^0_SK^0_L\pi^0$ invariant mass is shown in Fig. 4(a) for events with $\chi^2(K^0_SK^0_L\pi^0)$ in the signal (open histogram) and control (hatched) regions. The reconstruction efficiency as a function of mass is obtained by dividing the number of reconstructed MC events in each 50 MeV/c^2 mass interval by the number generated in that interval and is shown in Fig. 4(b). The effects of detector

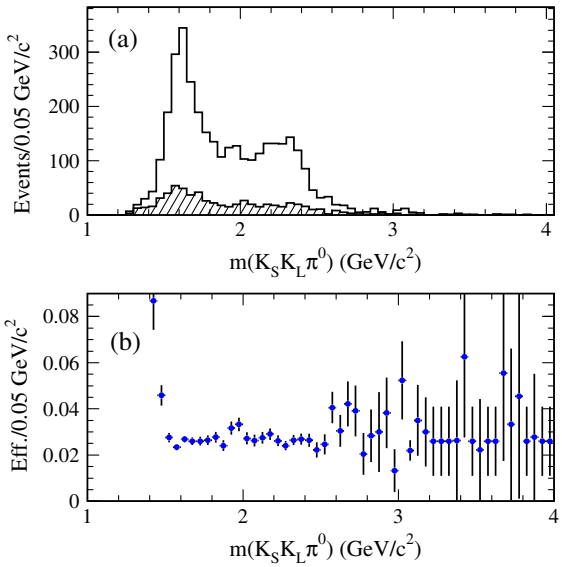

FIG. 4. (a) The reconstructed $K^0_SK^0_L\pi^0$ invariant mass distribution for MC-simulated signal events in the signal (open histogram) and control (hatched) regions of Fig. 3(a). (b) The net reconstruction efficiency from the simulation.

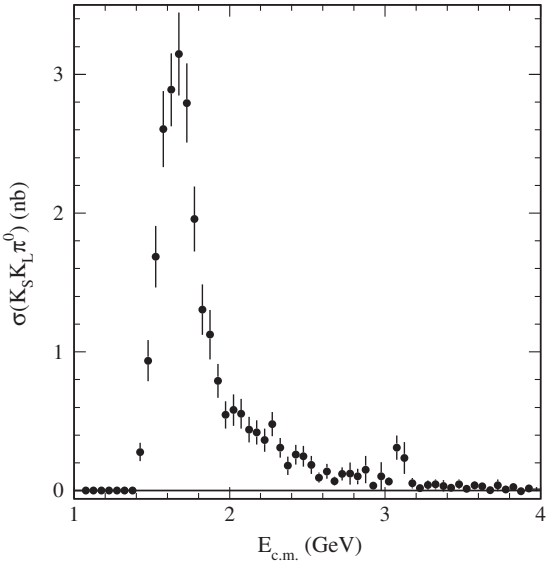

FIG. 5. The $e^+e^- \to K^0_S K^0_L \pi^0$ cross section. The error bars are statistical only.

resolution, about 25 MeV/c^2, are included in this efficiency. Below 1.5 GeV/c^2 the efficiency becomes very large, due to the rapidly changing cross section near threshold. Since the resolution is measured from the data and the shape of the threshold rise is well simulated, we apply no correction. Nevertheless, the backgrounds and the resolution-effect uncertainties are high in this region, so we do not quote a cross section measurement below 1.4 GeV/c^2, and we assign an additional 50% (30%) relative systematic uncertainty for the mass bin at 1.425 (1.475) GeV/c^2.

This efficiency is corrected for the data-MC differences evaluated in our previous studies. The ISR photon detection efficiency has been studied using $\mu^+\mu^-\gamma$ events [7], and we apply a polar-angle-dependent correction of typically $-1.5 \pm 0.5\%$ to the simulated efficiency. The K^0_S detection efficiency has been studied very carefully at *BABAR*, with data-MC differences in the efficiency determined as a function of the K^0_S direction and momentum. We apply a correction event by event, which introduces an overall correction of $+1.1 \pm 1.0\%$ to the efficiency. The π^0 reconstruction efficiency has been studied in *BABAR* using $\omega\gamma$ and $\omega\pi^0\gamma$ events, and the correction is found to be $(-3 \pm 1)\%$. The K^0_L detection requires a $(-6.1 \pm 0.6)\%$ correction [16]. In total, there is a $(-9.5 \pm 1.6)\%$ correction; this systematic uncertainty is small compared with that due to the backgrounds, described above.

D. The $e^+e^- \to K^0_S K^0_L \pi^0$ cross section

The cross section for e^+e^- annihilation into $K^0_S K^0_L \pi^0$ is calculated from

$$\sigma(K^0_S K^0_L \pi^0)(E_{\mathrm{c.m.}}) = \frac{dN_{K^0_S K^0_L \pi^0 \gamma}(E_{\mathrm{c.m.}})}{d\mathcal{L}(E_{\mathrm{c.m.}}) \cdot \epsilon(E_{\mathrm{c.m.}}) \cdot R}, \quad (1)$$

where $E_{\mathrm{c.m.}} \equiv m(K^0_S K^0_L \pi^0)$; $dN_{K^0_S K^0_L \pi^0 \gamma}$ is the number of selected, background-subtracted $K^0_S K^0_L \pi^0$ events in the interval $dE_{\mathrm{c.m.}}$; $\epsilon(E_{\mathrm{c.m.}}) = \epsilon^{\mathrm{MC}}(E_{\mathrm{c.m.}}) \cdot (1 + \delta_{\mathrm{corr}})$ is the simulated detection efficiency corrected for data-MC differences, as described above. The radiative correction R is unity within 1%, with an estimated precision of about 1%. The differential ISR luminosity $d\mathcal{L}(E_{\mathrm{c.m.}})$ associated with the interval $dE_{\mathrm{c.m.}}$ centered at an effective collision energy of $E_{\mathrm{c.m.}}$ is calculated using the leading-order formula (see, for example, Ref. [13]), and the systematic uncertainty associated with the luminosity determination is estimated to be 0.5%.

The cross section is shown as a function of energy in Fig. 5 and listed in Table I. There are no previous measurements for this final state. We do not quote the cross section from threshold (1.13 GeV) to 1.4 GeV, where it shows a sharp rise to a maximum value of about 3 nb near 1.7 GeV, presumably dominated by the $\phi(1680)$ resonance, and a slow decrease toward higher energies, perturbed by the J/ψ signal. Only statistical uncertainties are shown. The systematic uncertainty is dominated by background contributions and amounts to about 10% near the peak of

TABLE I. Summary of the $e^+e^- \to K_S K_L \pi^0$ cross section measurement. Uncertainties are statistical only.

$E_{\mathrm{c.m.}}$ (GeV)	σ (nb)	$E_{\mathrm{c.m.}}$ (GeV)	σ (nb)	$E_{\mathrm{c.m.}}$ (GeV)	σ (nb)	$E_{\mathrm{c.m.}}$ (GeV)	σ (nb)
1.425	0.28 ± 0.07	2.075	0.55 ± 0.11	2.725	0.12 ± 0.05	3.375	0.03 ± 0.04
1.475	0.94 ± 0.15	2.125	0.44 ± 0.09	2.775	0.12 ± 0.08	3.425	0.02 ± 0.01
1.525	1.68 ± 0.22	2.175	0.42 ± 0.09	2.825	0.10 ± 0.06	3.475	0.05 ± 0.03
1.575	2.60 ± 0.28	2.225	0.36 ± 0.08	2.875	0.15 ± 0.10	3.525	0.01 ± 0.03
1.625	2.89 ± 0.26	2.275	0.48 ± 0.09	2.925	0.04 ± 0.03	3.575	0.04 ± 0.03
1.675	3.15 ± 0.30	2.325	0.31 ± 0.07	2.975	0.10 ± 0.10	3.625	0.03 ± 0.03
1.725	2.79 ± 0.29	2.375	0.18 ± 0.07	3.025	0.06 ± 0.03	3.675	0.00 ± 0.01
1.775	1.96 ± 0.23	2.425	0.26 ± 0.07	3.075	0.31 ± 0.09	3.725	0.04 ± 0.04
1.825	1.30 ± 0.18	2.475	0.25 ± 0.08	3.125	0.24 ± 0.12	3.775	0.01 ± 0.01
1.875	1.12 ± 0.18	2.525	0.19 ± 0.06	3.175	0.05 ± 0.04	3.825	0.03 ± 0.02
1.925	0.79 ± 0.12	2.575	0.09 ± 0.04	3.225	0.02 ± 0.03	3.875	0.00 ± 0.01
1.975	0.55 ± 0.10	2.625	0.14 ± 0.05	3.275	0.04 ± 0.03	3.925	0.02 ± 0.02
2.025	0.58 ± 0.11	2.675	0.07 ± 0.03	3.325	0.05 ± 0.04	3.975	0.01 ± 0.01

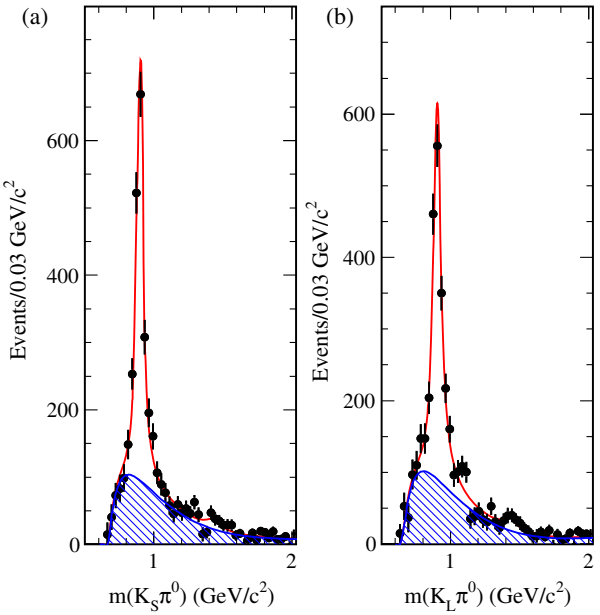

FIG. 6. The background-subtracted (a) $K^0_S\pi^0$ and (b) $K^0_L\pi^0$ invariant mass distributions in $e^+e^- \to K^0_S K^0_L \pi^0$ events. The curves represent the results of the fits described in the text, with the hatched areas representing the nonresonant components.

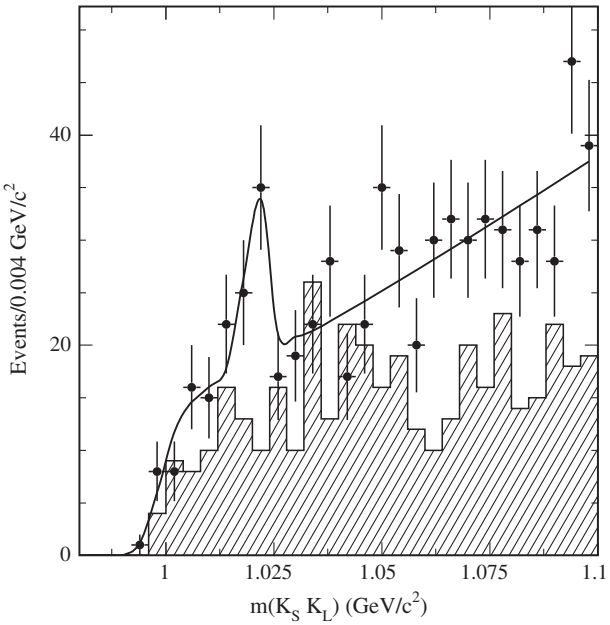

FIG. 7. The $K^0_S K^0_L$ invariant mass distribution in selected $K^0_S K^0_L \pi^0$ events (dots) and the background estimated from the control region (hatched histogram) of Fig. 3(a). The solid line represents the result of the fit described in the text.

the cross section (1.7 GeV), increasing roughly linearly with decreasing cross section to about 30% in the 2.5–3 GeV region, always similar in size to the statistical uncertainty. Above the J/ψ mass, statistics dominate the ~40% systematic uncertainty.

E. The $K^*(892)^0$ and $K_2^*(1430)^0$ contributions

Figure 6 shows the distributions of the fitted $K^0_S\pi^0$ and $K^0_L\pi^0$ invariant masses in the selected $K^0_S K^0_L \pi^0$ events, after background subtraction. Clear signals corresponding to the $K^*(892)^0$ resonance are visible, as well as indications of $K_2^*(1430)^0$ production.

We fit these distributions with a sum of two incoherent Breit-Wigner functions and a function describing the nonresonant contribution, yielding 1750 ± 84 $K^*(892)^0 \to K^0_S\pi^0$ decays, 1795 ± 56 $K^*(892)^0 \to K^0_L\pi^0$ decays, and a total of 145 ± 54 $K_2^*(1430)^0$ decays. The sum of these K^{*0} decays is consistent with the total number of $K^0_S K^0_L \pi^0$ events, indicating that the process is dominated by $K^{*0}\bar{K}^0 + \text{c.c.}$, and mostly $K^*(892)^0\bar{K}^0 + \text{c.c.}$, production.

Indeed, if we perform fits similar to those shown in Fig. 6 for events in each 0.05 GeV/c^2 interval of the $K^0_S K^0_L \pi^0$ invariant mass and sum the $K^*(892)^0 K^0_S$ and $K^*(892)^0 K^0_L$ yields, we obtain the $K^0_S K^0_L \pi^0$ mass distribution shown in Fig. 3(c) by the open circles. The errors are statistical only, and the difference between the number of $K^0_S K^0_L \pi^0$ events and the $K^*(892)^0\bar{K}^0$ contribution in each bin is less than the systematic uncertainty due to the background subtraction procedure.

F. The $\phi(1020)\pi^0$ contribution

Figure 7 shows the distribution of the fitted $K^0_S K^0_L$ invariant mass for the selected $K^0_S K^0_L \pi^0$ events before background subtraction (dots), along with the background (histogram) estimated from the $\chi^2(K^0_S K^0_L \pi^0)$ control region.

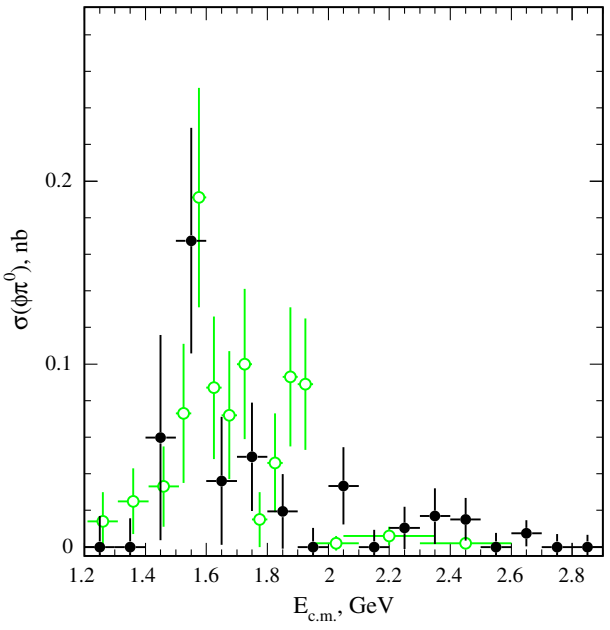

FIG. 8. The $e^+e^- \to \phi\pi^0$ cross section from this work (dots) compared with that obtained in the $K^+K^-\pi^0$ channel [15] (circles). The error bars are statistical only.

TABLE II. Summary of the $e^+e^- \to \phi\pi^0$ cross section measurement. Uncertainties are statistical only.

$E_{\rm c.m.}$ (GeV)	σ (nb)	$E_{\rm c.m.}$ (GeV)	σ (nb)
1.25	0.00 ± 0.02	2.15	0.00 ± 0.01
1.35	0.00 ± 0.02	2.25	0.01 ± 0.01
1.45	0.06 ± 0.06	2.35	0.02 ± 0.02
1.55	0.17 ± 0.06	2.45	0.02 ± 0.01
1.65	0.04 ± 0.03	2.55	0.00 ± 0.01
1.75	0.05 ± 0.03	2.65	0.01 ± 0.01
1.85	0.02 ± 0.02	2.75	0.00 ± 0.01
1.95	0.00 ± 0.01	2.85	0.00 ± 0.01
2.05	0.03 ± 0.02		

A $\phi(1020)$ signal is visible in the $K^0_S K^0_L \pi^0$ signal but not in the background. A fit with a Gaussian plus polynomial function yields a total of 29 ± 9 $\phi \to K^0_S K^0_L$ decays in $K^0_S K^0_L \pi^0$ events.

Fitting the $m(K^0_S K^0_L)$ distribution in 0.1 GeV/c^2 bins of the $K^0_S K^0_L \pi^0$ mass, we obtain a $\phi\pi^0$ invariant mass spectrum for the $K^0_S K^0_L \pi^0$ final state. Using Eq. (1) and the $\phi \to K^0_S K^0_L$ branching fraction [26], we calculate a cross section for this intermediate state, shown in Fig. 8 (dots) and listed in Table II. Only statistical uncertainties are shown. The systematic uncertainties of 10%–30% relative in this mass range are smaller than the statistical uncertainties.

The results are consistent with those observed in our previous study of the $K^+K^-\pi^0$ final state [15], also shown in Fig. 8 (circles). Together, our measurements suggest a possible resonant structure near 1.6 GeV/c^2 with isospin $I = 1$. The low cross section is expected, as the $\phi\pi^0$ channels are suppressed by the OZI rule.

VI. THE $K^0_S K^0_L \eta$ FINAL STATE

A. Final selection and backgrounds

We apply the same requirements on extra π^0's and $\chi^2(K^0_S K^0_L)$ as for the $K^0_S K^0_L \pi^0$ final state (see Sec. V) and consider the $\eta - K^0_L$ combination in each event with the best χ^2 under the $K^0_S K^0_L \eta\gamma$ hypothesis. Figure 9(a) shows the $\chi^2(K^0_S K^0_L \eta)$ distribution of the remaining events in the data (dots) compared with that of the signal simulation (open histogram). The simulated distribution is normalized to the data in the region $\chi^2(K^0_S K^0_L \eta) < 3$, where the contribution of higher-order ISR is small and the background contamination is lowest, but still amounts to about 10% of the signal. The cross-hatched and hatched areas represent the simulated contributions from non-ISR $q\bar{q}$ events and the sum of ISR $K^0_S K^0_L \pi^0$, ISR $K^0_S K^0_L$, and ISR $K^0_S K^0_L \pi^0\pi^0$ events, respectively; together, they account for about half of the excess of data over signal events at high values of χ^2.

We define a signal region $\chi^2(K^0_S K^0_L \eta) < 20$ and a control region $20 < \chi^2(K^0_S K^0_L \eta) < 40$ [vertical lines in Fig. 9(a)], containing 1829 data and 2518 signal-MC events and 1473 data and 495 signal-MC events, respectively. The $m(K^0_S K^0_L \eta)$ distribution for the events in the signal region is shown in Fig. 9(b) as points, along with the sum of the simulated background processes as the cross-hatched and hatched areas. Using events from the control region (see Sec. V B) we calculate the total background contribution, assumed to be dominated by ISR channels, and show it as the open histogram in Fig. 9(b).

We fit the total background with a smooth function to reduce fluctuations and use the result [curve in Fig. 9(b)] for the background subtraction. This yields a total of 864 ± 43

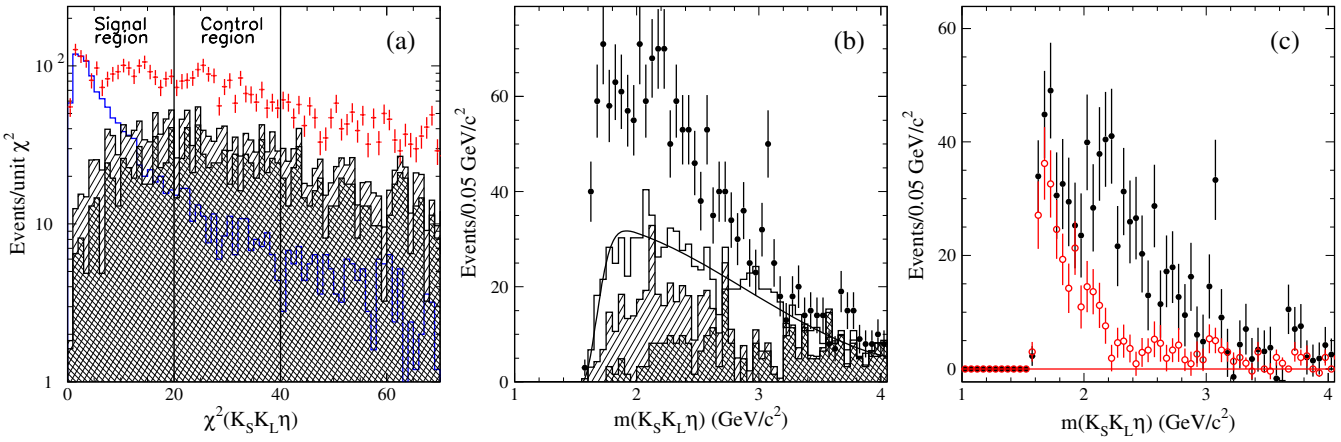

FIG. 9. (a) The four-constraint χ^2 distributions for data (points) and MC-simulated $K^0_S K^0_L \eta\gamma$ events (open histogram). The cross-hatched and hatched areas represent the simulated backgrounds from non-ISR $q\bar{q}$ events and the sum of ISR $K^0_S K^0_L \pi^0$, $K^0_S K^0_L$, and $K^0_S K^0_L \pi^0\pi^0$ events, respectively. (b) The $K^0_S K^0_L \eta$ invariant mass distribution for data events in the signal region (points). The cross-hatched and hatched areas represents simulated backgrounds from non-ISR $q\bar{q}$ and the sum of known ISR events, respectively, while the open histogram represents the total background, estimated from the control region. The curve shows the empirical fit used for background subtraction. (c) The $K^0_S K^0_L \eta$ invariant mass distribution after background subtraction (points). The open circles represent the contribution from the resonant process $e^+e^- \to \phi\eta \to K^0_S K^0_L \eta$ (see text).

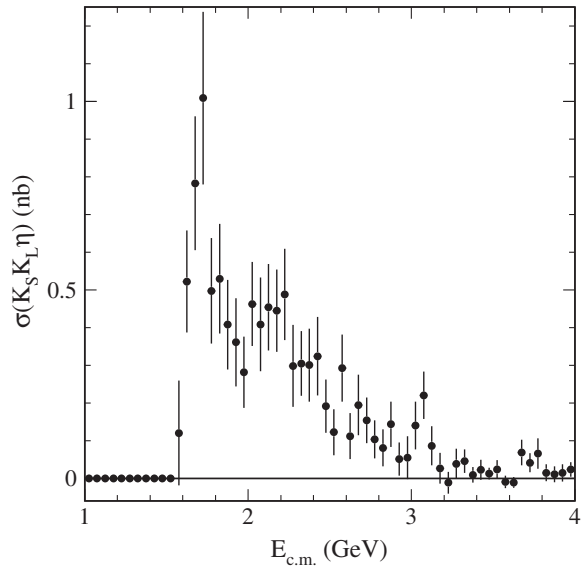

FIG. 10. The $e^+e^- \to K^0_S K^0_L \eta$ cross section.

signal events with masses between threshold and 4.0 GeV/c^2, with the mass distribution shown in Fig. 9(c). Again, we estimate the relative systematic uncertainty on the background as 30%, corresponding to an uncertainty on the cross section of about 15% for $m(K^0_S K^0_L \eta) < 2.2$ GeV/c^2, increasing roughly linearly to 30% at 3.0 GeV/c^2, and over 100% above 3.2 GeV/c^2.

B. Cross section for $e^+e^- \to K^0_S K^0_L \eta$

We calculate the $e^+e^- \to K^0_S K^0_L \eta$ cross section as a function of the effective c.m. energy using Eq. (1). The simulated efficiency is 1.6% and shows no dependence on the $K^0_S K^0_L \eta$ invariant mass. All efficiency corrections discussed in Sec. V D are applied; in particular, the same correction is applied to the η reconstruction efficiency as for the π^0.

The fully corrected cross section is shown in Fig. 10 and listed in Table III, with statistical uncertainties only. There are no other measurements for this final state. The cross section shows a steep rise from threshold at 1.6 GeV, a maximum value of about 1 nb near 1.7 GeV, and a decrease with increasing energy, punctuated by a clear J/ψ signal (discussed in Sec. VIII). The relative systematic uncertainty is dominated by the uncertainty of the backgrounds, totals 15% at the peak of the cross section, increases roughly linearly to about 30% at 3 GeV, and exceeds 100% at higher energies.

C. The $\phi(1020)\eta$ contribution

Figure 11 shows the background-subtracted $K^0_S K^0_L$ invariant mass distribution in $e^+e^- \to K^0_S K^0_L \eta$ events (dots), compared with that of simulated ISR $\phi\eta$ events (histogram). The two distributions are consistent at low mass values, and we simply take the number of events with $m(K^0_S K^0_L) < 1.05$ GeV/c^2 as an estimate of the $\phi\eta$ contribution. It totals 386 ± 20 events, with the $K^0_S K^0_L \eta$ invariant mass distribution shown in Fig. 9(c) as the open circles. The $\phi\eta$ channel dominates $K^0_S K^0_L \eta$ production for masses below about 2 GeV/c^2, but its contribution decreases rapidly for higher masses and shows no significant J/ψ signal.

Using these events, we calculate the $e^+e^- \to \phi\eta$ cross section, which is shown in Fig. 12 as the points. It is consistent with our previous measurement [15] in the $K^+K^-\eta$ final state (circles). Again, only statistical uncertainties are shown, and they are larger than the 15%–30% systematic uncertainties. We observe no significant structures in the $K^0_S\eta$ or in the $K^0_L\eta$ invariant mass distributions.

VII. THE $K^0_S K^0_L \pi^0 \pi^0$ FINAL STATE

A. Final selection and backgrounds

From all events with a K^0_S, a K^0_L and at least two nonoverlapping π^0 candidates, we consider the combination with the best value of $\chi^2(K^0_S K^0_L \pi^0 \pi^0)$, as described in Sec. IV. Since background candidates are not well suppressed using additional photon or π^0, no additional requirements are imposed. Figure 13(a) shows the $\chi^2(K^0_S K^0_L \pi^0 \pi^0)$ distribution of the data (dots), compared

TABLE III. Summary of the $e^+e^- \to K_S K_L \eta$ cross section measurement. Uncertainties are statistical only.

$E_{\rm c.m.}$ (GeV)	σ (nb)	$E_{\rm c.m.}$ (GeV)	σ (nb)	$E_{\rm c.m.}$ (GeV)	σ (nb)	$E_{\rm c.m.}$ (GeV)	σ (nb)
		2.075	0.41 ± 0.12	2.725	0.15 ± 0.06	3.375	0.01 ± 0.02
		2.125	0.45 ± 0.12	2.775	0.10 ± 0.05	3.425	0.02 ± 0.03
		2.175	0.44 ± 0.11	2.825	0.08 ± 0.05	3.475	0.01 ± 0.02
1.575	0.12 ± 0.14	2.225	0.49 ± 0.12	2.875	0.14 ± 0.06	3.525	0.02 ± 0.02
1.625	0.52 ± 0.14	2.275	0.30 ± 0.11	2.925	0.05 ± 0.04	3.575	-0.01 ± 0.02
1.675	0.78 ± 0.18	2.325	0.31 ± 0.09	2.975	0.05 ± 0.06	3.625	-0.01 ± 0.01
1.725	1.01 ± 0.23	2.375	0.30 ± 0.10	3.025	0.14 ± 0.06	3.675	0.07 ± 0.03
1.775	0.50 ± 0.14	2.425	0.32 ± 0.10	3.075	0.22 ± 0.06	3.725	0.04 ± 0.03
1.825	0.53 ± 0.14	2.475	0.19 ± 0.07	3.125	0.09 ± 0.05	3.775	0.07 ± 0.04
1.875	0.41 ± 0.12	2.525	0.12 ± 0.06	3.175	0.03 ± 0.04	3.825	0.01 ± 0.02
1.925	0.36 ± 0.12	2.575	0.29 ± 0.09	3.225	-0.01 ± 0.03	3.875	0.01 ± 0.02
1.975	0.28 ± 0.09	2.625	0.11 ± 0.06	3.275	0.04 ± 0.04	3.925	0.01 ± 0.02
2.025	0.46 ± 0.11	2.675	0.19 ± 0.08	3.325	0.05 ± 0.03	3.975	0.02 ± 0.02

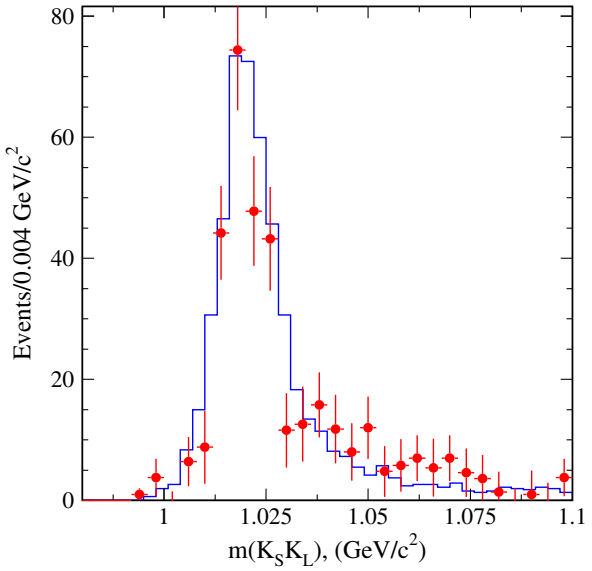

FIG. 11. The background-subtracted $K^0_S K^0_L$ invariant mass distribution in $e^+e^- \to K^0_S K^0_L \eta$ events (points), compared with that of simulated $e^+e^- \to \phi\eta$ events (histogram), normalized to number of experimental events.

with that of the signal simulation (open histogram). The simulated distribution is normalized to the data in the region $\chi^2(K^0_S K^0_L \pi^0\pi^0) < 5$, where the contribution of higher-order ISR is small and the background contamination is lowest, but still amounts to about 20% of the signal. The cross-hatched and hatched areas represent the simulated backgrounds from non-ISR $q\bar{q}$ and the sum of ISR $K^0_S K^0_L$, $K^0_S K^0_L \pi^0$, and $K^0_S K^0_L \eta$ events, respectively, where the latter two are normalized to our measurements reported above. Together, these account for a substantial fraction of the entries at high $\chi^2(K^0_S K^0_L \pi^0\pi^0)$ values.

We define a signal region $\chi^2(K^0_S K^0_L \pi^0\pi^0) < 30$ and a control region $30 < \chi^2(K^0_S K^0_L \pi^0\pi^0) < 60$ [vertical lines in Fig. 13(a)], containing 1748 data and 2465 signal-MC signal and 990 data and 517 signal-MC events, respectively. The $m(K^0_S K^0_L \pi^0\pi^0)$ distribution for the events in the signal region is shown in Fig. 13(b) as the points. The cross-hatched and hatched areas show the simulated contributions from non-ISR $q\bar{q}$ events and the sum of the ISR $K^0_S K^0_L$, $K^0_S K^0_L \pi^0$, and $K^0_S K^0_L \eta$ events, respectively.

We use a two-step procedure to subtract backgrounds in this final state. From all experimental distributions, we first subtract the normalized MC-simulated events just discussed. In the case of the $m(K^0_S K^0_L \pi^0\pi^0)$ distribution, we fit an empirical function to the sum of these, shown as the solid line in Fig. 13(b), and use that for a bin-by-bin subtraction. A similar procedure is applied to all other distributions, including that of $\chi^2(K^0_S K^0_L \pi^0\pi^0)$ [see Fig. 13(a)].

We then use events from the $\chi^2(K^0_S K^0_L \pi^0\pi^0)$ control region, after subtraction of the backgrounds just described, to calculate the remaining background in each bin of each distribution, as described in Sec. V B. We show this contribution to the $m(K^0_S K^0_L \pi^0\pi^0)$ distribution by the open squares in Fig. 13(b). We fit a smooth function to reduce fluctuations and use the results [dotted curve in Fig. 13(b)] to subtract the remaining background.

After subtraction of all backgrounds, we obtain 392 ± 55 signal events with masses between threshold and 4.0 GeV/c^2, distributed as shown in Fig. 13(c). We estimate the systematic uncertainty due to backgrounds to be about 25% of the signal for $m(K^0_S K^0_L \pi^0\pi^0) < 2.2$ GeV/c^2, increasing roughly linearly to 100% at 3.0 GeV/c^2, and everywhere smaller than the statistical uncertainty. There is no significant signal above about 2 GeV/c^2, apart from an indication of the J/ψ and $\psi(2S)$ signals in the 0.1 GeV/c^2 wide bins.

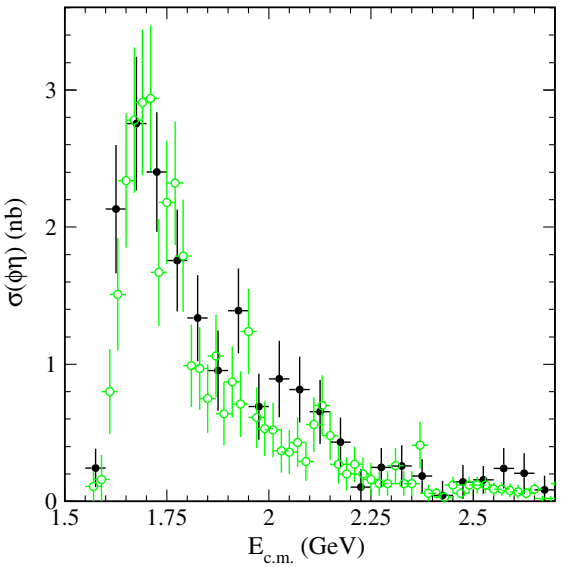

FIG. 12. The $e^+e^- \to \phi(1020)\eta$ cross section obtained from this work (solid dots), compared with the previous *BABAR* measurement in the $K^+K^-\eta$ final state [15] (open circles). Only statistical errors are shown.

B. Cross section for $e^+e^- \to K^0_S K^0_L \pi^0\pi^0$

We calculate the $e^+e^- \to K^0_S K^0_L \pi^0\pi^0$ cross section as a function of the effective c.m. energy $E_{\rm c.m.}$ using Eq. (1). The simulated efficiency is 1.5% and shows no dependence on the $K^0_S K^0_L \pi^0\pi^0$ invariant mass. All corrections discussed in Sec. V D are applied, plus an additional 3% for the detection of the second π^0. The fully corrected cross section is shown in Fig. 14 and listed in Table IV, with statistical uncertainties only. There are no other measurements for this final state.

The cross section shows a rise from a threshold at 1.4 GeV, a maximum value of about 0.5 nb near 1.8 GeV, and a decrease with increasing energy. Apart from a J/ψ and possibly a $\psi(2S)$ signal (discussed below), the cross

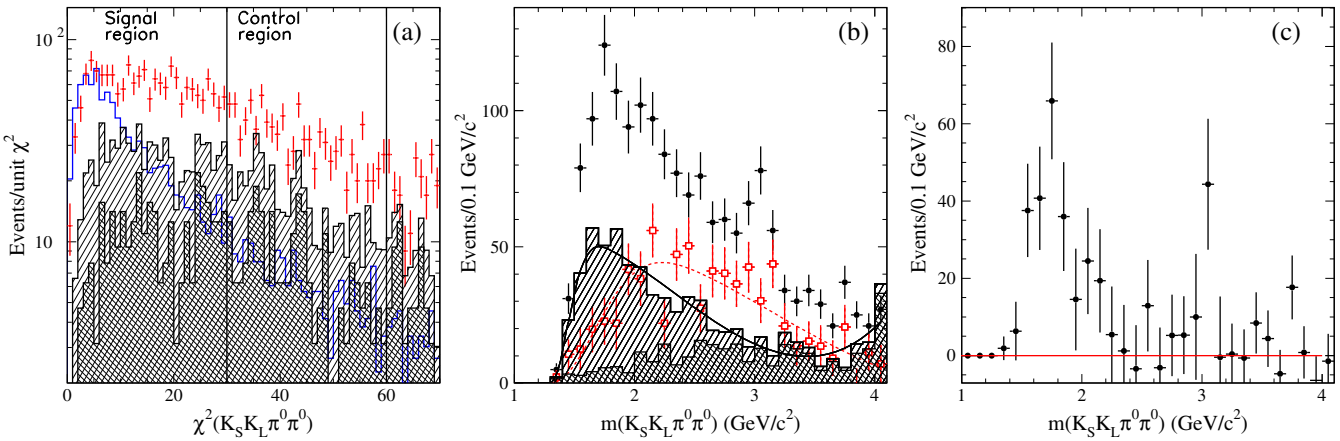

FIG. 13. (a) The five-constraint χ^2 distributions for data (points) and MC-simulated $K^0_SK^0_L\pi^0\pi^0\gamma$ events (open histogram). The cross-hatched and hatched areas represent the simulated backgrounds from non-ISR $q\bar{q}$ and the sum of ISR $K^0_SK^0_L$, $K^0_SK^0_L\pi^0$, and $K^0_SK^0_L\eta$ events, respectively. (b) The $K^0_SK^0_L\pi^0\pi^0$ invariant mass distribution for data events in the signal region of (a) (points). The cross-hatched and hatched areas represent the simulated contributions from non-ISR $q\bar{q}$ events and the sum of known ISR events, respectively, and the open squares represent the additional background estimated from the control region. The curves show the empirical fits used for background subtraction. (c) The $K^0_SK^0_L\pi^0\pi^0$ invariant mass distribution after subtraction of all backgrounds.

section is statistically consistent with zero above 2.2 GeV. The relative systematic uncertainty is dominated by the uncertainty of the backgrounds and totals 25% at the peak of the cross section, increasing linearly to about 60% at 2 GeV and 100% at higher energies.

C. The $K^*(892)^0$ and ϕ contributions

Figure 15 shows the $K^0_S\pi^0$ and the $K^0_L\pi^0$ invariant mass distributions for the selected $K^0_SK^0_L\pi^0\pi^0$ events after background subtraction (two entries per event). Signals corresponding to the $K^*(892)^0$ resonance are evident, but the statistics are not sufficient to study them in detail.

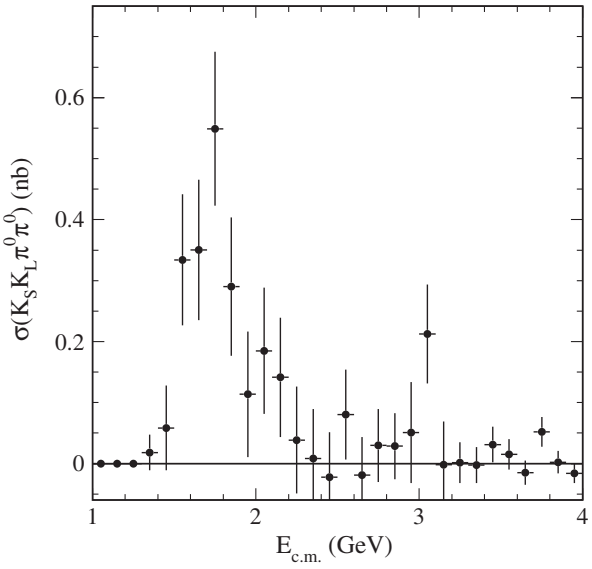

FIG. 14. The $e^+e^- \to K^0_SK^0_L\pi^0\pi^0$ cross section.

As an exercise, we fit these distributions with a sum of a Breit-Wigner function and a smooth function describing the nonresonant contribution, yielding 190 ± 44 $K^*(892)^0 \to K^0_S\pi^0$ decays and 171 ± 32 $K^*(892)^0 \to K^0_L\pi^0$ decays. There is no indication from the scatter plot (not shown) of any contribution from the $e^+e^- \to K^*(892)^0\bar{K}^*(892)^0$ reaction, and the sum of the two $K^*(892)$ yields is less than the total number of $K^0_SK^0_L\pi^0\pi^0$ events, limiting any such contribution to half the signal events. This pattern is consistent with the dominance of the $e^+e^- \to K^*(892)^0K^-\pi^+ + \text{c.c.}$ processes seen in our previous measurement of the $e^+e^- \to K^+K^-\pi^+\pi^-$ reaction [11].

TABLE IV. Summary of the $e^+e^- \to K^0_SK^0_L\pi^0\pi^0$ cross section measurement. Uncertainties are statistical only.

$E_{c.m.}$ (GeV)	σ (nb)	$E_{c.m.}$ (GeV)	σ (nb)
1.3500	0.018 ± 0.029	2.7500	0.029 ± 0.059
1.4500	0.059 ± 0.070	2.8500	0.028 ± 0.054
1.5500	0.334 ± 0.108	2.9500	0.051 ± 0.083
1.6500	0.350 ± 0.115	3.0500	0.213 ± 0.081
1.7500	0.549 ± 0.126	3.1500	-0.002 ± 0.071
1.8500	0.290 ± 0.113	3.2500	0.002 ± 0.033
1.9500	0.113 ± 0.103	3.3500	-0.002 ± 0.029
2.0500	0.185 ± 0.104	3.4500	0.031 ± 0.029
2.1500	0.141 ± 0.098	3.5500	0.015 ± 0.025
2.2500	0.038 ± 0.088	3.6500	-0.015 ± 0.020
2.3500	0.008 ± 0.081	3.7500	0.052 ± 0.024
2.4500	-0.022 ± 0.073	3.8500	0.002 ± 0.018
2.5500	0.080 ± 0.074	3.9500	-0.016 ± 0.016
2.6500	-0.019 ± 0.062		

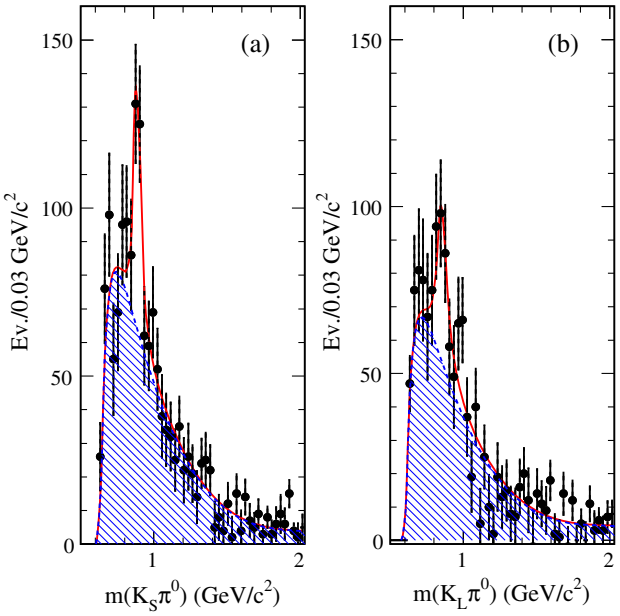

FIG. 15. The (a) $K^0_S\pi^0$ and (b) $K^0_L\pi^0$ invariant mass distributions for selected $K^0_SK^0_L\pi^0\pi^0$ events in the data (points). The curves represent the results of the fits described in the text, with the hatched areas representing the nonresonant components.

Fitting the $K^0_SK^0_L$ invariant mass distribution (not shown), we observe 71 ± 16 events from the $e^+e^-\to\phi(1020)\pi^0\pi^0\to K^0_SK^0_L\pi^0\pi^0$ process. This is consistent with expectations from our measurement in the $K^+K^-\pi^0\pi^0$ mode [11] but with substantially lower precision.

VIII. THE CHARMONIUM REGION

Figure 16 shows expanded views of the mass distributions in Figs. 3(b), 9(b), and 13(b), respectively, in the 2.5–4.0 GeV/c^2 mass region without any background subtraction. There are clear J/ψ signals in all three distributions and indications of $\psi(2S)$ signals in Figs. 16(b) and 16(c). Fitting the distribution in Fig. 16(a) with the sum of the simulated J/ψ signal shape and a second-order polynomial function yields 182 ± 21 $J/\psi\to K^0_SK^0_L\pi^0$ decays. No signal from the $\psi(2S)\to K^0_SK^0_L\pi^0$ decay is observed (<8 events at 90% C.L.). Fitting the other two distributions with the sum of simulated J/ψ and $\psi(2S)$ signal shapes and a second-order polynomial function yields 45 ± 10 $J/\psi\to K^0_SK^0_L\eta$ decays, 47 ± 11 $J/\psi\to K^0_SK^0_L\pi^0\pi^0$ decays, 16 ± 5 $\psi(2S)\to K^0_SK^0_L\eta$ decays, and 14 ± 6 $\psi(2S)\to K^0_SK^0_L\pi^0\pi^0$ decays.

Using the corrected simulated efficiencies described above and the differential luminosity, we calculate the products of the J/ψ [$\psi(2S)$] electronic width and branching fractions to these modes and list them in Table V. Using the PDG value of $\Gamma_{ee}(J/\psi)=5.55$ keV [$\Gamma_{ee}(\psi(2S))=2.35$ keV] [26], we obtain the corresponding branching fractions, also presented in Table V. Systematic uncertainties of typically 5% arise from the corrections to the simulated efficiencies, discussed in Sec. V C, and variations of the signal shape.

These are the first observations of these three J/ψ decay modes. Our $K^0_SK^0_L\pi^0$ branching fraction can be compared with existing measurements of similar modes $\mathcal{B}(J/\psi\to K^+K^-\pi^0)=(2.8\pm0.8)\times10^{-3}$ [27] and $\mathcal{B}(J/\psi\to K^\pm K^0_S\pi^\mp)=(2.6\pm0.7)\times10^{-3}$ [28]. The data are consistent with the expectation from isospin conservation that they are equal. Our other two measured branching fractions are consistent with existing results for the corresponding modes involving charged kaons [26], of $\mathcal{B}(J/\psi\to K^+K^-\eta)=(0.85\pm0.14)\times10^{-3}$ and $\mathcal{B}(J/\psi\to K^+K^-\pi^0\pi^0)=(2.35\pm0.41)\times10^{-3}$, respectively.

There are no previous observations of $\psi(2S)$ decays into any of these modes. Our measurements indicate the presence of the $\psi(2S)\to K^0_SK^0_L\eta$ and $K^0_SK^0_L\pi^0\pi^0$ decay modes at just over three and two standard deviations,

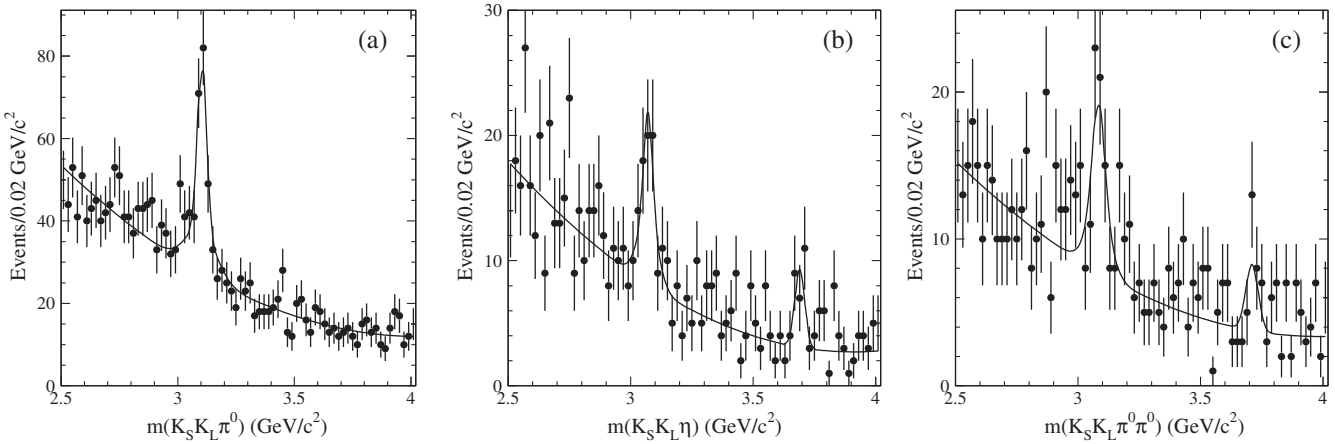

FIG. 16. Expanded views of the invariant mass distributions in the charmonium mass region for the (a) $K^0_SK^0_L\pi^0$, (b) $K^0_SK^0_L\eta$, and (c) $K^0_SK^0_L\pi^0\pi^0$ final states. The lines represent the results of the fits described in the text.

TABLE V. Summary of the J/ψ and $\psi(2S)$ branching fractions obtained in this analysis.

Measured quantity	Measured value (eV)			Calculated branching fractions (10^{-3}) This work			Previous	
$\Gamma_{ee}^{J/\psi}\cdot\mathcal{B}_{J/\psi\to K_S^0K_L^0\pi^0}$	11.4	1.3	0.6	2.06	0.24	0.10	···	
$\Gamma_{ee}^{J/\psi}\cdot\mathcal{B}_{J/\psi\to K_S^0K_L^0\eta}$	8.0	1.8	0.4	1.45	0.32	0.08	···	
$\Gamma_{ee}^{J/\psi}\cdot\mathcal{B}_{J/\psi\to K_S^0K_L^0\pi^0\pi^0}$	10.3	2.3	0.5	1.86	0.43	0.10	···	
$\Gamma_{ee}^{J/\psi}\cdot\mathcal{B}_{J/\psi\to K^*(892)^0\bar{K}^0+\text{c.c.}}\cdot\mathcal{B}_{K^*(892)^0\to K^0\pi^0}$	6.7	0.9	0.4	1.20	0.15	0.06	···	
$\Gamma_{ee}^{J/\psi}\cdot\mathcal{B}_{J/\psi\to K_2^*(1430)^0\bar{K}^0+\text{c.c.}}\cdot\mathcal{B}_{K_2^*(1430)\to K^0\pi^0}$	2.4	0.7	0.1	0.43	0.12	0.02	<4	[26]
$\Gamma_{ee}^{\psi(2S)}\cdot\mathcal{B}_{\psi(2S)\to K_S^0K_L^0\pi^0}$		<0.7			<0.3		···	
$\Gamma_{ee}^{\psi(2S)}\cdot\mathcal{B}_{\psi(2S)\to K_S^0K_L^0\eta}$	3.14	1.08	0.16	1.33	0.46	0.07	···	
$\Gamma_{ee}^{\psi(2S)}\cdot\mathcal{B}_{\psi(2S)\to K_S^0K_L^0\pi^0\pi^0}$	2.92	1.27	0.15	1.24	0.54	0.06	···	

respectively, and we give in Table V an upper limit at the 90% C.L on the $K_S^0K_L^0\pi^0$ mode.

A. Internal structure of the $J/\psi\to K_S^0K_L^0\pi^0$, $K_S^0K_L^0\eta$, and $K_S^0K_L^0\pi^0\pi^0$ decays

We consider $K_S^0K_L^0\pi^0$ events in the charmonium region with a $K_S^0\pi^0$ or $K_L^0\pi^0$ invariant mass within 0.15 GeV/c^2 of the nominal $K^*(892)^0$ or $K_2^*(1430)^0$ mass and show their $K_S^0K_L^0\pi^0$ invariant mass distributions in Figs. 17(a) and 17(b), respectively. Fits using simulated J/ψ signal shapes and polynomial backgrounds yield 106 ± 13 $J/\psi\to(K^*(892)^0\bar{K}^0+\text{c.c.})\to K_S^0K_L^0\pi^0$ events and 37 ± 11 $J/\psi\to(K_2^*(1430)^0\bar{K}^0+\text{c.c.})\to K_S^0K_L^0\pi^0$ events. For each of these intermediate states we calculate the product of its J/ψ branching fraction, $\Gamma_{ee}^{J/\psi}$, and the relevant branching fractions for the intermediate resonances and list the values in Table V. Using $\Gamma_{ee}^{J/\psi}=5.55$ eV [26] we calculate the corresponding products of branching fractions.

This first measurement of $\mathcal{B}(J/\psi\to(K_2^*(1430)^0\bar{K}^0+\text{c.c.})\to K^0\bar{K}^0\pi^0)$ is consistent with the existing upper limit of 4×10^{-3} [26]. According to isospin relations, the $J/\psi\to(K^*(892)^0\bar{K}^0+\text{c.c.})\to K_S^0K_L^0\pi^0$ decay rate should be the same as the existing world average of $1.97\pm0.20\times10^{-3}$ [26] for the charged-kaon decay chain $J/\psi\to(K^*(892)^+\bar{K}^-+\text{c.c.})\to K^+K^-\pi^0$, and a factor of 2 lower than the $3.2\pm0.4\times10^{-3}$ [26] observed in the $\bar{K}^0K^+\pi^-+\text{c.c.}$ final state. Our result is consistent with the latter expectation and 2.5 standard deviations below the former. In Sec. VI C we noted that the $\phi\eta$ contribution to the J/ψ signal in the $K_S^0K_L^0\eta$ mode is very small. We estimate 5 ± 3 events, corresponding to $\mathcal{B}(J/\psi\to\phi\eta)=(0.52\pm0.32)\times10^{-3}$, which is consistent with the PDG [26] value of $(0.75\pm0.08)\times10^{-3}$. The J/ψ signal in the $K_S^0K_L^0\pi^0\pi^0$ mode has high background [see Fig. 16(c)], and we are unable to quantify the contributions from the $K^*(892)^0K^0\pi^0$ and $\phi\pi^0\pi^0$ intermediate states with reasonable accuracy. The $J/\psi\to\phi\pi^0\pi^0$ decay rate is relatively well measured [26], dominated by our previous measurement in the $K^+K^-\pi^0\pi^0$ final state.

IX. SUMMARY

We have presented studies of the processes $e^+e^-\to K_S^0K_L^0\pi^0$, $e^+e^-\to K_S^0K_L^0\eta$, and $e^+e^-\to K_S^0K_L^0\pi^0\pi^0$ at center-of-mass energies below 4 GeV, using events with initial-state radiation collected with the *BABAR* detector. The cross sections for all three processes are measured for the first time, over the energy range from threshold to 4 GeV, and their resonant structure is studied.

The $e^+e^-\to K_S^0K_L^0\pi^0$ cross section is measured with 10%–30% systematic uncertainty below 3 GeV and is similar in shape to the $e^+e^-\to K^+K^-\pi^0$ cross section [15]. It is dominated by resonant, quasi-two-body intermediate states. The $K^*(892)^0\bar{K}^0+\text{c.c.}$ processes account for about 90% of the cross section, and there are few-percent contributions from the $K^*(1430)^0\bar{K}^0+\text{c.c.}$ and $\phi\pi^0$

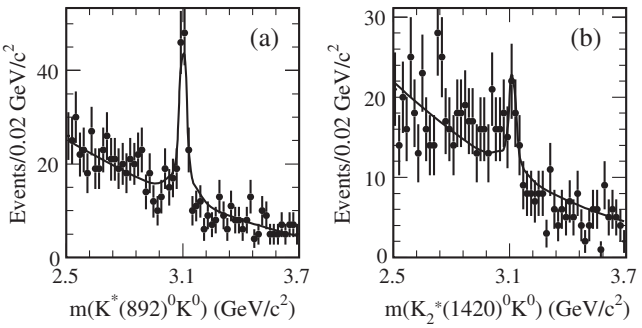

FIG. 17. The $K_S^0K_L^0\pi^0$ invariant mass distributions for events in which the $K_S^0\pi^0$ or $K_L^0\pi^0$ mass is within 0.15 GeV/c^2 of (a) the nominal $K^*(892)^0$ mass or (b) the nominal $K_2^*(1430)^0$ mass. The lines represent the results of the fits described in the text.

processes. The cross section for the latter is consistent with that measured previously in the $K^+K^-\pi^0$ final state.

The $e^+e^- \to K^0_S K^0_L \eta$ cross section is measured with 15%–30% systematic uncertainty below 3 GeV and is similar to the $e^+e^- \to K^+K^-\eta$ cross section [15]. The $\phi\eta$ intermediate state dominates below 2.0 GeV and contributes up to 3.0 GeV, and its cross section is consistent with that measured previously in the $K^+K^-\eta$ final state. No other intermediate states are observed, and nonresonant $K^0_S K^0_L \eta$ production is substantial in the 2.2–3.0 GeV range.

The $e^+e^- \to K^0_S K^0_L \pi^0\pi^0$ cross section is measured with 25%–60% systematic uncertainty below 3 GeV and is consistent with the $e^+e^- \to K^0_S K^0_S \pi^+\pi^-$ cross section [16]. Its $E_{\rm c.m.}$ behavior is similar in shape to the $e^+e^- \to K^+K^-\pi^+\pi^-$, $K^0_S K^0_L \pi^+\pi^-$, and $K^+K^-\pi^0\pi^0$ cross sections but factors of about 8, 2, and 1.5 smaller, respectively. There are substantial, but not dominant, contributions from the $K^*(892)^0\bar{K}^0\pi^0$, $K^*(1430)^0\bar{K}^0\pi^0$ and $\phi(1020)\pi^0\pi^0$ intermediate states. These are hard to quantify but are consistent with expectations from our previous studies of the $e^+e^- \to K^+K^-\pi^+\pi^-$ and $K^+K^-\pi^0\pi^0$ processes. We see no evidence for any $K^{*0}\bar{K}^{*0}$ intermediate states, also consistent with the low rates we have observed in final states involving charged kaons.

We observe the $J/\psi \to K^0_S K^0_L \pi^0$, $K^0_S K^0_L \eta$, and $K^0_S K^0_L \pi^0\pi^0$ decays for the first time and measure the product of the J/ψ electronic width and branching fraction to each of these modes. We study the resonant structure of these decays and obtain measurements of the $J/\psi \to K^*(892)^0\bar{K}^0 + \text{c.c.}$ and $J/\psi \to K_2^*(1430)^0\bar{K}^0 + \text{c.c.}$ branching fractions times $\Gamma_{ee}^{J/\psi}$. In addition, we observe the $\psi(2S) \to K^0_S K^0_L \eta$ and $\psi(2S) \to K^0_S K^0_L \pi^0\pi^0$ decays for the first time and measure the products of the $\psi(2S)$ electronic width and the corresponding branching fractions.

ACKNOWLEDGMENTS

We are grateful for the extraordinary contributions of our PEP-II2 colleagues in achieving the excellent luminosity and machine conditions that have made this work possible. The success of this project also relies critically on the expertise and dedication of the computing organizations that support *BABAR*. The collaborating institutions wish to thank SLAC for its support and the kind hospitality extended to them. This work is supported by the U.S. Department of Energy and National Science Foundation, the Natural Sciences and Engineering Research Council (Canada), the Commissariat à l'Energie Atomique and Institut National de Physique Nucléaire et de Physique des Particules (France), the Bundesministerium für Bildung und Forschung and Deutsche Forschungsgemeinschaft (Germany), the Istituto Nazionale di Fisica Nucleare (Italy), the Foundation for Fundamental Research on Matter (Netherlands), the Research Council of Norway, the Ministry of Education and Science of the Russian Federation, Ministerio de Economía y Competitividad (Spain), the Science and Technology Facilities Council (United Kingdom), and the Binational Science Foundation (U.S.–Israel). Individuals have received support from the Marie-Curie IEF program (European Union) and the A. P. Sloan Foundation (USA).

[1] V. N. Baier and V. S. Fadin, Phys. Lett. B **27**, 223 (1968).
[2] A. B. Arbuzov, E. A. Kuraev, N. P. Merenkov, and L. Trentadue, J. High Energy Phys. 12 (1998) 009.
[3] S. Binner, J. H. Kühn, and K. Melnikov, Phys. Lett. B **459**, 279 (1999).
[4] M. Benayoun, S. I. Eidelman, V. N. Ivanchenko, and Z. K. Silagadze , Mod. Phys. Lett. A **14**, 2605 (1999).
[5] M. Davier, S. Eidelman, A. Höcker, and Z. Zhang, Eur. Phys. J. C **31**, 503 (2003); M. Davier, A. Höcker, B. Malaescu, and Z. Zhang, Eur. Phys. J. C **71**, 1 (2011); K. Hagiwara, R. Liao, A. D. Martin, D. Nomura, and T. Teubner, J. Phys. G **38**, 085003 (2011).
[6] B. Aubert *et al.* (*BABAR* Collaboration), Phys. Rev. D **69**, 011103 (2004).
[7] B. Aubert *et al.* (*BABAR* Collaboration), Phys. Rev. Lett. **103**, 231801 (2009); J. P. Lees *et al.* (*BABAR* Collaboration), Phys. Rev. D **86**, 032013 (2012).
[8] J. P. Lees *et al.* (*BABAR* Collaboration), Phys. Rev. D **88**, 032013 (2013).
[9] J. P. Lees *et al.* (*BABAR* Collaboration), Phys. Rev. D **88**, 072009 (2013).
[10] B. Aubert *et al.* (*BABAR* Collaboration), Phys. Rev. D **71**, 052001 (2005).
[11] B. Aubert *et al.* (*BABAR* Collaboration), Phys. Rev. D **86**, 012008 (2012).
[12] B. Aubert *et al.* (*BABAR* Collaboration), Phys. Rev. D **73**, 052003 (2006).
[13] B. Aubert *et al.* (*BABAR* Collaboration), Phys. Rev. D **70**, 072004 (2004).
[14] B. Aubert *et al.* (*BABAR* Collaboration), Phys. Rev. D **76**, 092005 (2007).
[15] B. Aubert *et al.* (*BABAR* Collaboration), Phys. Rev. D **77**, 092002 (2008).
[16] J. P. Lees *et al.* (*BABAR* Collaboration), Phys. Rev. D **89**, 092002 (2014).

[17] J. P. Lees *et al.* (*BABAR* Collaboration), Nucl. Instrum. Methods Phys. Res., Sect. A **726**, 203 (2013).
[18] B. Aubert *et al.* (*BABAR* Collaboration), Nucl. Instrum. Methods Phys. Res., Sect. A **479**, 1 (2002); B. Aubert *et al.* (*BABAR* Collaboration), Nucl. Instrum. Methods Phys. Res., Sect. A **729**, 615 (2013).
[19] H. Czyż and J. H. Kühn, Eur. Phys. J. C **18**, 497 (2001).
[20] A. B. Arbuzov, E. A. Kuraev, G. V. Fedotovich, N. P. Merenkov, V. D. Rushai, and L. Trentadue, J. High Energy Phys. 10 (1997) 001.
[21] M. Caffo, H. Czyż, and E. Remiddi, Nuovo Cimento A **110**, 515 (1997); Phys. Lett. B **327**, 369 (1994).
[22] E. Barberio, B. van Eijk, and Z. Was, Comput. Phys. Commun. **66**, 115 (1991).
[23] S. Agostinelli *et al.* (GEANT Collaboration), Nucl. Instrum. Methods Phys. Res., Sect. A **506**, 250 (2003).
[24] T. Sjöstrand, Comput. Phys. Commun. **82**, 74 (1994).
[25] S. Jadach and Z. Was, Comput. Phys. Commun. **85**, 453 (1995).
[26] C. J. Beringer *et al.* (Particle Data Group Collaboration), Phys. Rev. D **86**, 010001 (2012).
[27] M. E. B. Franklin *et al.* (Mark II Collaboration), Phys. Rev. Lett. **51**, 963 (1983).
[28] F. Vanucci *et al.* (Mark I Collaboration), Phys. Rev. D **15**, 1814 (1977).
[29] M. N. Achasov *et al.* (SND Collaboration), Phys. Rev. D **63**, 072002 (2001).
[30] R. R. Akhmetshin *et al.* (CMD-2 Collaboration), Phys. Lett. B **695**, 412 (2011).